Aerospace Science and Technology 93 (2019) 105320

Contents lists available at ScienceDirect

Aerospace Science and Technology

www.elsevier.com/locate/aescte

Investigation on flutter stability of the DLR-F19/SACCON configuration

Guido Voss [a,*], Dominik Schaefer [a], Cyrille Vidy [b]

[a] Institute of Aeroelasticity, DLR (German Aerospace Center), Bunsenstrasse 10, 37073 Goettingen, Germany
[b] Department for Structural Dynamics and Aeroelasticity, Airbus Defence and Space, Rechliner Strasse, 85077 Manching, Germany

ARTICLE INFO

Article history:
Received 30 January 2019
Received in revised form 29 May 2019
Accepted 31 May 2019
Available online 1 August 2019

ABSTRACT

In the present work, flutter stability studies of an unmanned flying-wing configuration are presented. For this purpose, different fidelity modeling methods (DLM, CFD-Euler and CFD-RANS) are considered. The dependence of flutter speeds on altitude and Mach number is examined, showing that aerodynamic potential-based methods cannot predict aerodynamic phenomena such as flow detachment occurring at high angles of attack. In this respect, it is important that flutter investigations industry-oriented calculation methods are compared with the results obtained by high-fidelity CFD methods.

1. Introduction

Flutter is considered one of the most critical phenomena in aviation. Accordingly, in the development and design of new aircraft configurations, emphasis is placed on flutter stability prediction in order to avoid its occurrence during flight.

The dynamic aeroelastic characteristics of flying-wing configurations such as the F19/SACCON configuration are not fully understood yet. In the history of aviation, major accidents have repeatedly occurred due to changes in the design of aircraft. Especially in the period between the World War I and World War II, when monoplane aircraft should replace the classic biplane aircraft for their better flight characteristics, there were tragic accidents as the result of flutter instabilities on wings and control surfaces. This has increasingly attracted the attention of aeroelasticians in order to better understand this phenomenon [1]. Flying-wing configurations have a higher short-term natural frequency compared to that of classic aircraft configurations. This is due to the lower pitching moment of inertia with respect to classical configurations with empennage. Thus, the natural frequencies become closer and the influence of rigid body modes, which can contribute to the flutter mechanism, increases. In this case, it may cause rigid body modes to cause a flutter event before classic flutter such as bending-torsional flutter occurs, a phenomenon known as “Body Freedom Flutter”. The demonstrator X-56A, developed by NASA, specifically examines this flutter phenomenon ([2], [3]).

Flutter is an aeroelastic instability phenomenon which involves the interaction of structural characteristics of an aircraft configuration with the unsteady aerodynamic forces of the surrounding flow. Aircraft components have certain elastic oscillation modes such as flexural vibration modes, torsional modes, in-plane modes, each with characteristic natural frequencies or eigenfrequencies. In addition, six rigid-body modes are considered for a free-flying configuration. These are the displacement in the x- and y-direction, the displacement in the z-direction (heave mode), the rotation about the x axis (roll mode), the y axis (pitch mode) and the z axis (yaw mode). All rigid-body modes have a structural eigenfrequency of $f = 0$ Hz.

The action of the aerodynamic unsteady forces changes the frequency and damping properties of the system eigenmodes as a function of the speed of the aircraft. Typically, when the frequencies of particular eigenmodes approach (when increasing the flight speed), the eigenmodes may overlap with a resulting decreased of the mode damping value, potentially causing an instability. This ultimately leads to a complete structural failure. An example of a flutter mechanism is the classic bending torsion flutter that couples bending and torsional modes.

Particularly in the case of flying wing configurations, as in the case of the F19 model (Fig. 1) considered here, so-called Body-Freedom-Flutter can occur, in which case the rigid-body modes interact with the elastic modes leading to the instability.

In the development of new aircraft flutter stability analysis have to be considered. Flutter calculations are carried out for a combination of different flight conditions. For this purpose, “fast” methods which allow a high number of calculations in a reasonable time are typically used. For instance, aerodynamic methods based on the potential theory may be chosen. However, these methods do not allow for the description of aerodynamic phenomena such as flow separation, presence of shocks, three-dimensional vortex-

* Corresponding author.
E-mail address: guido.voss@dlr.de (G. Voss).

https://doi.org/10.1016/j.ast.2019.105320

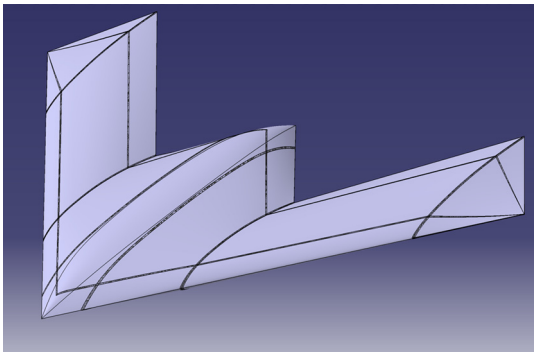

Fig. 1. DLR-F19/SACCON configuration.

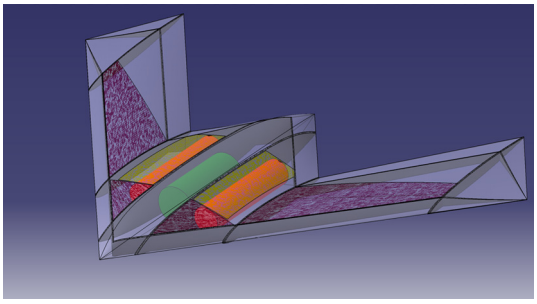

Fig. 2. CAD model of the F19 configuration.

dominated flow and boundary layer effects. Nevertheless, these fast methods allow for a first assessment of the flutter stability limits.

In this paper the flutter predictions obtained by the use of fast methods are compared with those obtained by considering high-fidelity methods (Euler or RANS methods) for the computation of the unsteady aerodynamic forces.

2. Configuration aspects

2.1. Mission aspects

The design of the DLR-F19/SACCON configuration relies on a set of mission definitions and the ability to remain largely invisible to the opposing radar. The planform of the F19 configuration is therefore designed in a lambda construction in order to achieve the best possible stealth properties. A possible mission trajectory provides the aircraft approach to the operation area at high altitude. In the target area, the aircraft must be able to execute highly agile flight maneuvers.

The sizing of the F19 configuration is done according to these specifications. Due to the high agility capabilities the maximum take-off weight is limited to 15 tons. At the same time, the aircraft must be of sufficient size to accommodate the required amounts of fuel, payload, as well as avionics, structure and engine.

2.2. Geometric model (CAD)

The DLR-F19/SACCON model is a lambda-style flying wing configuration with a span of $s = 15{,}375$ m and a total planform area of $A = 77$ m^2. The sweep angle is 53° both at the leading edge and at the trailing edge of the fuselage, see Fig. 2. The reference chord length is $c = 4.79$ m. The leading edge in the area of the fuselage is designed to be sharp with a strong initially increasing radius of curvature in the spanwise direction and a slightly decreasing value approaching the wing tip. This creates complex flow vortex patterns over the configuration, especially at high angles of attack.

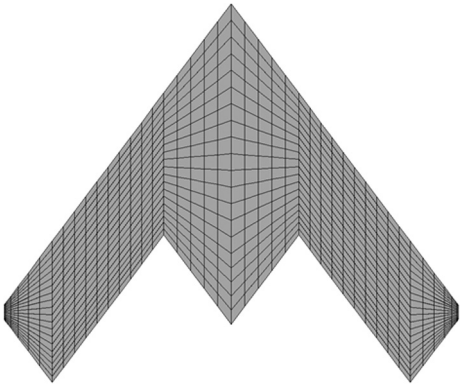

Fig. 3. DLM grid.

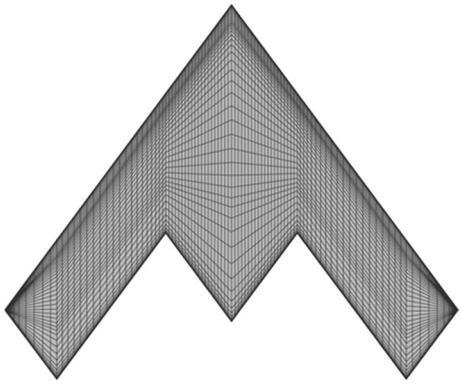

Fig. 4. High-fidelity surface grid (Euler).

2.3. Aerodynamic model

In order to investigate the aerodynamic properties of the F19 model two computational grids were generated for the high-fidelity methods. The investigations with the fast methods NASTRAN (DLM for Doublet Lattice Method in subsonic, ZONA51 in supersonic) and ZAERO (ZONA6, resp. ZONA7) were carried out on a planar grid as shown in Fig. 3. The planform is divided into boxes with an aspect ratio value close to 2. Again, fast methods are not able to describe shock phenomena, flow separation or vortices.

Concerning the high-fidelity AER-NS and AER-SDNS Euler calculations method based on the Euler equations, the considered structured volume mesh of the baseline DLR-F19 configuration was generated with ICEM Hexa from ANSYS and has about 0.8 million cells. The geometric discretization over the body surface is shown in Fig. 4.

For the RANS calculations, a hybrid computational grid was created, see Fig. 5. The grid was manufactured using the grid generation tools ICEM Hexa and Centaur [4]. The actual model configuration was provided with a block-structured hexahedral grid (shown in blue in Fig. 5). This variant was chosen to allow optimized resolution of aerodynamic structures (e.g., vortices, separations) for further calculations. In order to avoid too many points and elements in the farfield, unstructured tetrahedral elements were generated (shown in yellow in Fig. 5). Both grids were connected to the Chimera approach of the TAU flow solver software ([5,6]) to form an overall computational grid, which consists of 5.9 million points and a total of 11.1 million elements. The boundary layer was resolved with 40 hexahedral layers, where the first wall distance to the body surface was chosen so that calculations with Reynolds numbers up to about $90 \cdot 10^6$ provides $y+$ values small enough.

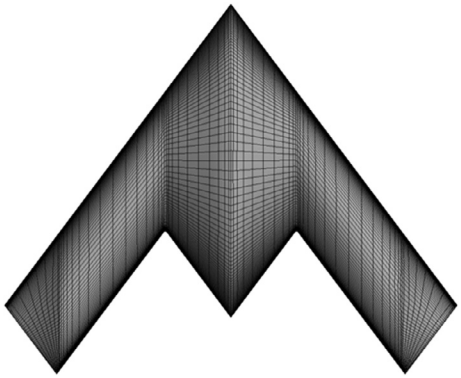

(a) CFD RANS surface grid discretization

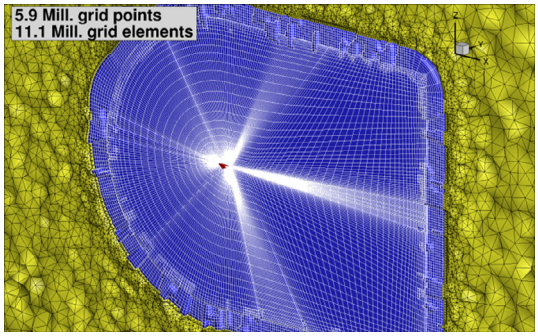

(b) Overall grid for RANS computations (Chimera approach)

Fig. 5. CFD mesh configuration. (For interpretation of the colors in the figure(s), the reader is referred to the web version of this article.)

Table 1
DLR-F19 baseline mass cases.

Key	Total mass [kg]	Description
M1	7361	No fuel, no payload
M2	12509	Max. fuel, no payload
M3	14509	Max. fuel, max. payload
M4	9361	No fuel, max. payload
M5	11941	Half fuel, max. payload

2.4. Aeroelastic model

The finite element model of the DLR-F19 consists of 8054 nodes and is not being condensed for the flutter analyses [7]. Five "baseline mass cases" are presented with the corresponding properties as listed in Table 1. For the investigations presented in this paper the mass case M5 (half fuel, max. payload) was selected. This choice is based on the fact that the fuel masses have a great influence on the flutter properties of this configuration. Considering cases of maximum refueling (M2, M3) results in different flutter behavior (see [8]). In addition, the mass case M5 is considered to be most representative in terms of possible future missions.

Table 2 shows the considered eigenmodes for the CFD-Euler and the potential methods. The grey shaded modes highlight the modes used for the CFD-RANS computations.

The interpolation between the structural and aerodynamic grids was done using Infinite Plate Spline ([8,17]). Only for the AER-SDNS computations the Thin Plate Spline was used. For this purpose, different parameter sets were defined for the spline of each component in order to be able to model the geometrical discontinuities between wing and control surfaces. In [8] it was shown that this has a great influence on the proper prediction of the flutter behavior and has therefore to be taken into account.

Table 2
Eigenmodes and eigenfrequencies of F19 (mass case M5); grey highlighted eigenmodes were considered for the RANS-computations.

No	Eigenmode	Eigenfrequency [Hz]
1	x-lateral	0.0
2	y-lateral	0.0
3	heave	0.0
4	roll	0.0
5	pitch	0.0
6	yaw	0.0
7	first symmetric wing bending	9.61
8	first antimetric wing bending	10.24
9	first symmetric in-plane with wing bending	17.96
10	first symmetric wing torsion	19.59
11	first antisymmetric wing torsion	20.99
12	first antisymmetric in-plane with wing bending	26.46
13	first symmetric wing torsion with wing bending	27.46
14	second antisymmetric wing bending with fuselage roll	29.40
15	Third symmetric wing bending with first symmetric engine heave mode	34.67
16	Second antisymmetric wing torsion with first antisymmetric engine heave mode	38.97
17	Third symmetric wing bending with fuselage bending	44.30
18	Second symmetric wing torsion with fuselage bending and first symmetric engine heave mode	46.01
19	Third antisymmetric wing bending with fuselage roll and first antisymmetric engine heave mode	47.03
20	Wing tip bending mode	55.34

2.5. Aeroelastic stability envelope

The aeroelastic stability envelope of the DLR-F19 configuration is determined according to the MIL-A-8870C specification [9]. The configuration has to be flutter free over an enlarged envelope by 15% the maximum equivalent airspeed (EAS) for both constant Mach number and constant altitude. The Equivalent Air Speed is calculated with Eq. (12).

$$v_{EAS} = v_{TAS} \times \sqrt{\frac{\rho_h}{\rho_0}} \tag{12}$$

where v_{TAS} is the True Speed, ρ_0 the density at sea level and ρ_h the density at considered altitude level.

Fig. 6 shows the design speeds and the enlarged flutter envelope. This configuration is then required to be flutter free at altitudes between $h = -2419$ m and $h = 13716$ m and for Mach numbers below $\mathrm{Ma} = 1.115$.

2.6. Numerical tools

Both aerodynamic potential-based methods (NASTRAN, ZAERO) and high-fidelity aerodynamic methods (AER-SDNS, TAU) have been considered for the flutter stability computations.

Since 1985, the developer of the ZAERO software package, ZONA, has been devoting a research effort for the development of unsteady aerodynamic methods for aeroelastic applications. The first ZONA software product for supersonic lifting surface unsteady aerodynamics is the ZONA51 code. ZONA 51 employs the acceleration-potential approach for thin-wing type of lifting surfaces [10]. This acceleration-potential approach is the outgrowth from the Harmonic Gradient Method (HGM) developed by Chen and Liu 1985 [11]. Today, ZONA51 is the industrial standard method for supersonic lifting surface unsteady aerodynamics in NASTRAN [12]. ZONA7 generalizes ZONA51 for the wing-body configuration [13]. Its lifting surface method is identical to ZONA51

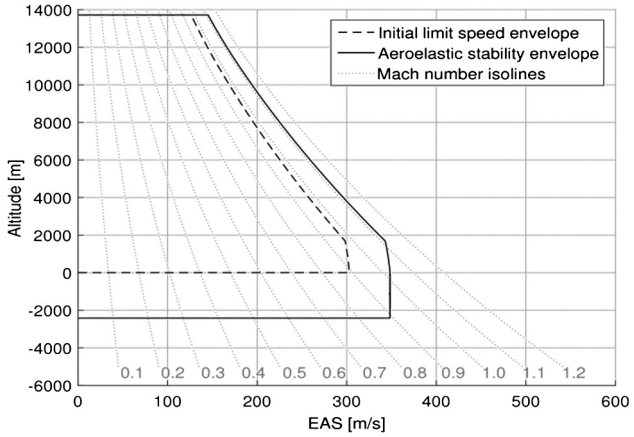

Fig. 6. Aeroelastic stability envelope.

but its body aerodynamic capability enables ZONA7 to model realistic aircraft configurations including the external stores. ZONA6 is the subsonic counterpart of ZONA7 except that it includes the important body-wake effects for fuselage and stores [14].

NASTRAN uses DLM and ZONA51 as the basis for calculation, while the ZAERO software package uses the ZONA6 and ZONA7 modules.

2.6.1. NASTRAN modal analysis

The generalized mass and stiffness structural matrices are obtained by the modal analysis provided by the solution sequence SOL 103 in NASTRAN. By applying the Lanczos method, the real eigenvalue problem (Eq. (1)) is solved for both rigid-body and elastic structural modes [15]. In Eq. (1), $[K]$ denotes the structural stiffness matrix, $[M]$ the structural mass matrix (both in the physical reference frame), $\lambda_i = \omega_i^2$ the real eigenvalue, and $\{\phi_i\}$ the real eigenvector.

$$\big([K] - \lambda_i[M]\big)\{\phi_i\} = 0 \tag{1}$$

Combining the mode shape vectors $\{\phi_i\}$ into a mode shape matrix $[\Phi]$ with

$$[\Phi] = \big[\{\phi_1\}, \{\phi_2\}, \ldots \{\phi_n\}\big] \tag{2}$$

and n being the number of mode shapes, leads to the generalized mass and stiffness matrices in the modal reference frame, viz.

$$[\overline{M}] = [\Phi]^T[M][\Phi] \tag{3}$$

$$[\overline{K}] = [\Phi]^T[K][\Phi] \tag{4}$$

In the presence of stress-free modes, as is the case for rigid-body modes, the Lanczos method yields eigenfrequencies which are only numerical zeros of the order 10^{-4} Hz. In addition, the rigid-body eigenvectors do not appear along the global reference axis. This does not influence the flutter results but yet the rigid-body eigenfrequencies are replaced by $f = 0.0$ Hz and the corresponding mode shapes generated kinematically using the SUPORT bulk data entry.

2.6.2. DLM/ZONA6

The potential flow aerodynamic methods DLM and ZONA6 solve the steady and unsteady tree-dimensional linearized small disturbance potential equations (LSDPE), which read

$$\big(1 - M_\infty^2\big)\psi_{0xx} + \psi_{0yy} + \psi_{0zz} = 0 \tag{5}$$

$$\big(1 - M_\infty^2\big)\psi_{1xx} + \psi_{1yy} + \psi_{1zz} - 2\frac{M_\infty}{a_\infty}\psi_{1xt} - \frac{1}{a_\infty^2}\psi_{1tt} = 0 \tag{6}$$

where M_∞ is the freestream Mach number, a_∞ the speed of sound, and ψ_0 and ψ_1 the steady and unsteady potentials, respectively. Eq. (5) is the steady and Eq. (6) the unsteady LSDPE. By assuming simple harmonic motion at the circular frequency ω with constant amplitude, Eq. (6) can be transformed into an integral equation which is then solved by discretizing according to the panel method. By subdividing the configuration into small trapezes (aerodynamic boxes), this method computes the aerodynamic influence coefficient matrix $[AIC(jk, M)]$ which relates the downwash at each aerodynamic box to the pressure coefficient difference at the aerodynamic boxes, viz.

$$\{\Delta c_p\} = \big[AIC(jk, M_\infty)\big]^{-1}\{w\} \tag{7}$$

with j the imaginary unit and k the reduced frequency

$$k = \frac{\omega L_{ref}}{U_\infty} \tag{8}$$

where L_{ref} is the reference length (typically half of the mean aerodynamic chord) and U_∞ the freestream velocity. The resulting aerodynamic forces are interpolated on the structural model via a splining matrix $[G]$ and projected into the generalized coordinates corresponding to the structural modes (in vacuum) according to

$$[Q\,k, M_\infty)] = [\Phi]^T[G]^T[S]\big[AIC(jk, M)\big]^{-1}[G][\Phi] \tag{9}$$

2.6.3. Unsteady Euler solver AER-SDNS

AER-NS is a flow solver which solves the compressible Euler or RANS equations on structured meshes. It has been developed at the Technical University of Munich by the Chair of Aerodynamics and Fluid Mechanics [16].

The solver AER-SDNS linearizes the CFD equations around a steady-state as obtained b AER-NS. Thus, the linear effect of surface deformations or of atmospheric gust disturbances can be determined in the form of generalized aerodynamic matrices in the frequency domain. These matrices can then be used in the flutter solver to in order to compute the aeroelastic stability.

The AER-NS and AER-SDNS solvers have been developed in cooperation with the Structural Dynamics and Aeroelasticity department of Airbus Defence and Space in order for both solvers to deliver aerodynamic inputs for aeroelastic problems in an efficient and robust way. A more detailed description of these methods together with their potential usages can be found in [19], [16] and [20].

2.6.4. Unsteady RANS solver TAU/FlowSimulator

2.6.4.1. Methods All RANS calculations were carried out with the DLR-TAU flow solver. A well-converged steady solution is first required for the subsequent computation of the unsteady aerodynamic flow.

The unsteady pulse calculations are performed with the FlowSimulator [21]. This software package possesses different modules that can be used to perform aerodynamic and aeroelastic simulations. In particular forced motion calculations in which prescribed structural and rigid-body mode motions can be imposed on the considered geometry. For the calculations presented here, the one-equation turbulence model SAO according to Spalart-Allmaras [22] was used. The temporal discretization takes place via the implicit backward Euler method ([5], [6]) whereas the spatial discretization is performed with a central second-order schema. The CFL number, which is represented as a measure of the numerical speed by the computational grid, is set conservatively to the value 1. All calculations were performed without multigrid convergence acceleration techniques, as they produce a deteriorated convergence behavior in this configuration.

2.6.4.2. Process For unsteady calculations pulse calculations were carried out. Instead of producing a steady-state response for each harmonic frequency, the pulse calculation provides results at many discrete frequencies instead. The pulse can be regarded as the superposition of several sine waves at different frequencies, thus covering a wide frequency spectrum. In order to avoid that the spectrum of the pulse becomes zero for some particular frequency range below the structural eigenfrequencies under consideration, a special pulse shape has been imposed. The increasing part of the pulse is described by a 1-cos function and the decreasing one by a polynomial of 5th order. The pulse amplitude is chosen to be very small in order to ensure the linear behavior of the flow solver.

For the coupling between the structural and aerodynamic models, the spline matrix is applied to each generalized coordinate separately and stored in a preprocessing step.

By means of the deformation tool within FlowSimulator, the surface deformation is extended into the volume finite volume mesh for each particular generalized coordinate. The time history of the aerodynamic forces and moments produced by the pulse is then recorded. In order to filter out the influence of numerical errors from the result, a so-called zero calculation with a corresponding zero pulse amplitude is subtracted from the unsteady computation.

For the calculation of the flutter stability the generalized aerodynamic forces (GAFs) corresponding to the rigid-body and structural modes are required in the frequency domain. They are calculated as the sum of the scalar product from the calculated unsteady aerodynamic forces with the displacement matrix Δx Eq. (10) for the corresponding generalized coordinate. The elements of the GAF matrix GAF_{ij} are complex-valued after transformation into the frequency domain by means of the Fast Fourier Transformation (FFT) of the time domain signals. They can be obtained by dividing the Fourier transform of the element Q_{ij} by the Fourier transform of the pulse input signal IN_{pulse} (Eq. (11)).

$$Q_{ij} = \sum_{i=0}^{N} (F_{pulse} - F_{zero})_i \cdot \Delta x_j \tag{10}$$

$$GAF_{ij} = \frac{FFT(Q_{ij})}{FFT(IN_{pulse})} \tag{11}$$

For the present flutter analyses a non-matched flutter (regarding the Reynolds number) solution using the p–k-method and a range of Mach numbers from Ma = 0.2 to Ma = 1.2 was produced. More details are shown for the case of Ma = 0.8. The airspeed (EAS) is increased from $v = 40$ m/s in increments of $\Delta v = 5$ m/s up to a final value of $v = 900$ m/s. The air density corresponds to the value at Mean Sea Level (MSL) according to the International Standard Atmosphere (ISA) and therefore amounts to $\rho = 1.225$ kg/m^3 [23]. The used reduced frequencies (Eq. (8)) are based on the reference chord length of $c = 4.79$ m.

3. Results

3.1. NASTRAN/DLM/ZONA51 computations

Once the rigid-body and structural modes have been obtained, the eigenmodes with an eigenfrequency value above $f = 55$ Hz present local spatial deformations and are not taken into account. Thus, a total of 20 eigenmodes (including the 6 rigid-body modes) are considered for the subsequent flutter analyses.

The NASTRAN solution 145 provides several flutter solution methods corresponding to various modifications of the k- and the p–k-method. For the present analyses, the p–k-method as described in [24] is used in combination with the DLM for subsonic potential flows and ZONA51 for supersonic potential flows. The calculations were carried out with a set of 12 reduced frequency values ranging from 0.01 to 3.6.

The resulting flutter curves for the reference mass case M5 and Mach number of Ma = 0.8 are shown in Fig. 7. The modal frequency together with damping values is plotted versus the increasing true airspeed. Two flutter crossings from negative to positive values can be identified at flight velocities of roughly 725 m/s (Symmetric Body-Freedom-Flutter mechanism) and 730 m/s (Antisymmetric flutter mechanism) respectively. At a significantly higher velocity compared to the other two flutter crossings (approx. 825 m/s), a sign change of the damping factors reveals a third flutter mechanism (Symmetric in-plane flutter mechanism). The small damping curve slope prevents this mechanism to be identified visually. Besides coalescing frequency lines of certain elastic modes between 10 Hz and 20 Hz at the flutter crossings together with an increasing frequency and decreasing damping of a rigid-body mode can be seen at velocities up to 730 m/s. At higher speeds, this mode presents a higher damping value and a reduced frequency, indicating its contribution to the first flutter mechanism. Fig. 10(a)–(c) show the corresponding flutter eigenmode.

3.2. CFD computations

3.2.1. Steady computations

As described in Sections 2.6.3 and 2.6.4, the steady calculations were carried out with the DLR-TAU flow solver (RANS) and the AER-NS flow solver (Euler). The different boundary conditions imposed in the flow solvers are listed below:

- Seven Mach numbers, three of them in the subsonic range, two in the transonic range, two in the supersonic range (Ma = 0.2, 0.4, 0.6, 0.8, 0.9, 1.1, 1.2)
- Angle of attack: $\alpha = 1.0°$ (all RANS Mach numbers, Euler Mach number Ma = 0.8)
- Angle of attack: $\alpha = 0.0°$ (all Euler Mach numbers)
- Three altitudes each ($h = 0$ m, $h \approx 1600$ m, $h \approx 13000$ m)

The Reynolds numbers corresponding to the RANS calculations range from $4.7 \cdot 10^6$ up to $133.9 \cdot 10^6$ according to Mach number and altitude level.

3.2.2. Unsteady computations (AER-SDNS)

The unsteady Euler calculations were carried out with the AER-SDNS flow solver with the following parameters:

- All steady conditions considered for AER-NS
- 12 reduced frequencies from 0.01 to 3.6 (the same as for ZONA6/DLM)
- Surface deformations due to the first 20 structural eigenmodes of the M5 mass configuration, including the 6 rigid-body modes (the same as for ZONA6/DLM)

The aerodynamic flow solution is not dependent on the altitude value because of the inviscid assumption of the Euler equations. Thus, the computed dataset can be used for the whole altitude range of the flight-envelope of the DLR-F19 configuration.

3.2.3. Unsteady computations (RANS)

As described in Section 2.6.4, the FlowSimulator tool together with DLR-TAU flow solves have been used for the unsteady computations. For this purpose, the respective generalized coordinate corresponding to each eigenmode was subjected to a pulse of small amplitude and the aerodynamic response was marched in the time domain. As stated in Section 2.6.4.2 a zero calculation with a zero

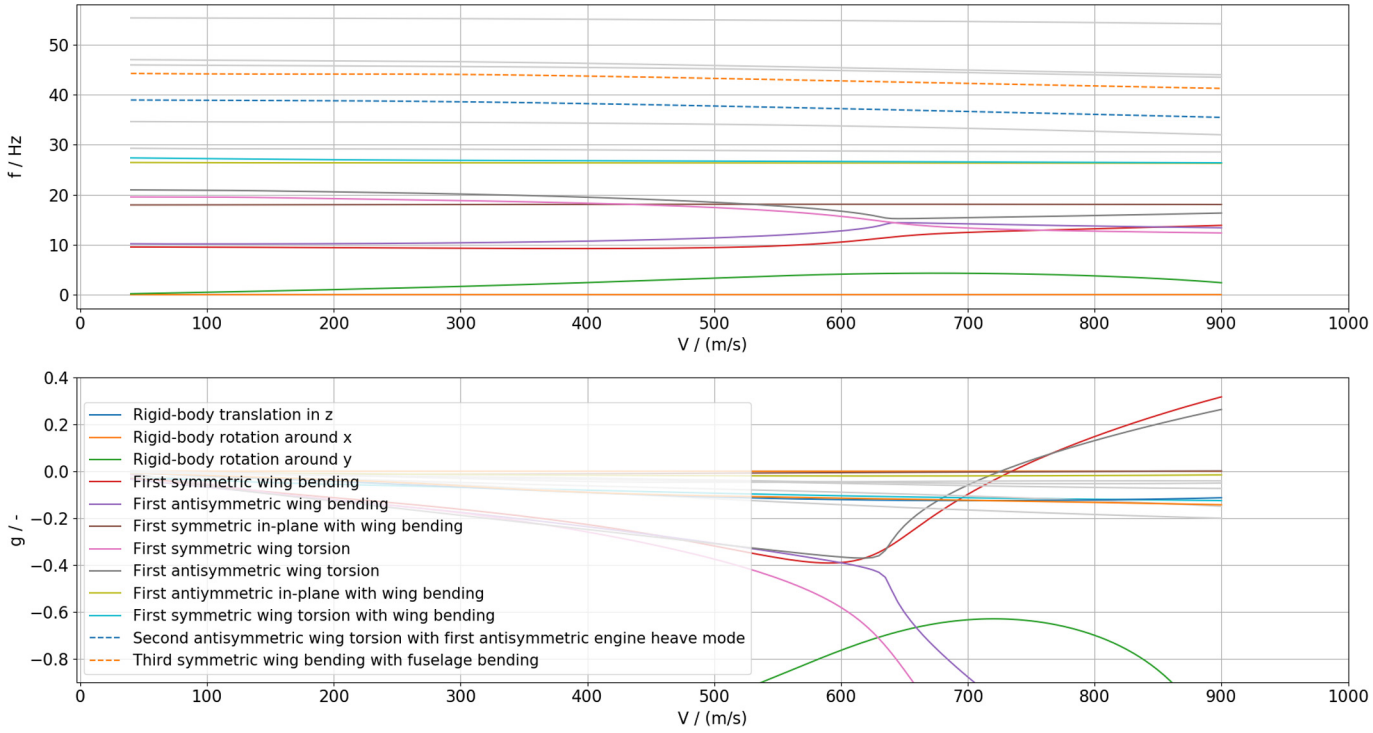

Fig. 7. NASTRAN-based flutter curves (fast method or low-fidelity).

pulse amplitude was substracted to each computation in order to reduce the numerical noise.

A total of eight vibration modes were used for the RANS calculations. These are the two rigid-body modes corresponding to the heave and pitch motions and the first six elastic modes of the F19 configuration (see the grey shaded parts of Table 2).

The range of the reduced frequency is chosen between $k = 0.0$ and $k = 0.5$ with a spacing of $\Delta k = 0.05$. For this frequency resolution, a total of 1280 time steps were used for each calculation. This corresponds to a time step size of $\Delta t = 0.00173$ s (at Ma $= 0.8$, sea-level). The number of internal iterations per time step was set to 300. This was a compromise between a good convergence behavior at each time step and a limited computing time. The computational time was of approximately seven days for each Mach number. The pulse amplitude was set to $\Delta\alpha = 0.001°$ for pitch, $\Delta q = 0.001$ m for heave and elastic modes (hinge line at $x = 6$ m). The steady angle of attack of $\alpha = 1°$ was chosen as a representative horizontal cruise trimmed flight condition. With this value a good convergence of the steady computations could be achieved A main element to determine the flutter stability is the matrix of generalized unsteady aerodynamic forces (GAF). The procedure for calculating the GAF matrix is described in Chapter III.

To ensure a linear behavior of the overall system, it is necessary to choose the pulse amplitude sufficiently small. Fig. 8 shows the real and the imaginary part of an element of the generalized aerodynamic matrix for Ma $= 0.2$ (sea-level). The orange line shows the same element for a pulse amplitude 10 times higher than that for the black line. A good match between both is achieved in the low to middle frequency range. Only in the higher frequency range the peak amplitude for the smaller pulse amplitude can be explained by the influence of numerical noise, yet a linear behavior is guaranteed.

Fig. 9 shows an element of the GAF corresponding to a pitch mode input and projected in the same generalized coordinate as real part and imaginary parts. In this case, the GAF element at low frequencies represents the slope of the pitching moment polar $dc_m/d\alpha$. There is a reasonable agreement between the results obtained by ZONA6 and the Euler and RANS computations.

The results of the GAF curves from the Euler calculations for the angle of attack $\alpha = 0°$ differ to a much lesser extent from the results for $\alpha = 1°$ for the different aerodynamic methods, even though not shown here. This is expected because of the presence of more complex flow phenomena at higher angle of attacks.

3.2.4. Flutter computation

The reference flutter solution was obtained with the p–k solver of the software package NASTRAN. In addition, further flutter solvers were investigated, the results of which should agree with the p–k solver of the reference solution ([15], [16], [17]). The p–k solvers available in the ZAERO software package (ZONA6, ZONA7) were used for the results of the RANS calculations and the one available in the Airbus Defense & Space in-house tool IDEA for the Euler results.

For this purpose, a so-called non-matched flutter analysis was performed. This means that the aerodynamic influence coefficients (AIC) matrix is computed at a given Mach number. Based on this AIC matrix, the flutter speed and the corresponding frequency are obtained for a defined range of the freestream velocity.

For each of the underlying calculation methods and the range of parameters considered three different flutter mechanisms were identified:

- Symmetric Body-Freedom-Flutter (BFF) mechanism
- Symmetric in-plane flutter mechanism
- Antisymmetric flutter mechanism

The corresponding flutter curves are shown in Fig. 10 for a Mach number of Ma $= 0.8$ for ZONA6 calculations. On the right side the frequency and damping evolutions over the speed (TAS) are shown. The lines for the frequency plot are plotted as solid for values of the mode participation of 100% and dashed for values less than 100%. As before, the flutter occurs when the damping value changes from negative to positive. This is further clarified by

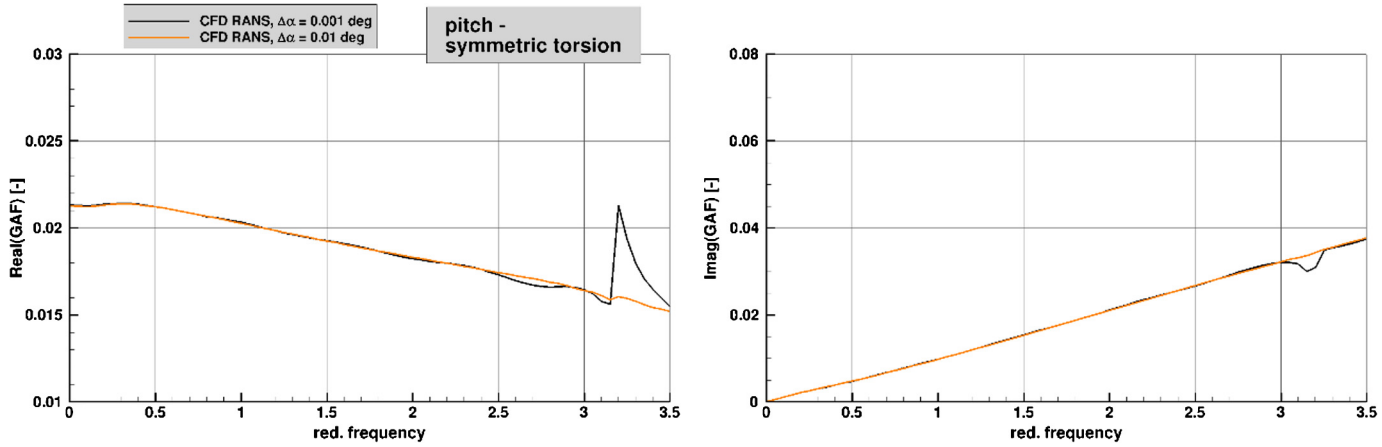

Fig. 8. Comparison of RANS GAF elements with different pulse amplitude and ZONA6 GAF element.

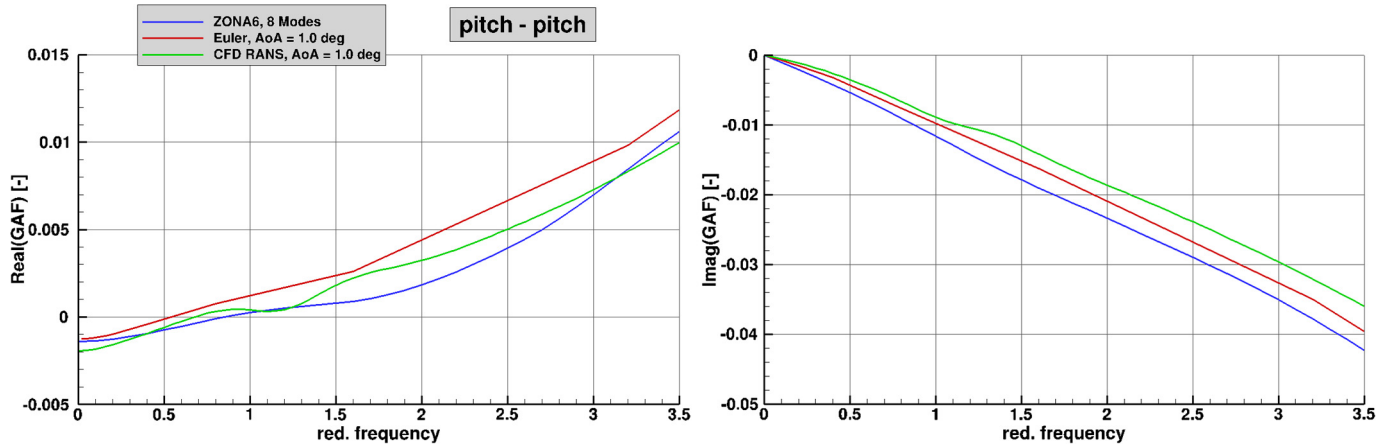

Fig. 9. Element of the GAF-Matrix (pitch on pitch) with the real part (left hand side) and the imaginary part (right hand side).

an approximation of the frequency curves of the modes involved in the flutter mechanism, which is also referred to as coupling.

Fig. 10a and 10b show the identified Symmetric Body-Freedom-Flutter and Antisymmetric flutter modes obtained with the ZAERO computations considering the first eight eigenmodes as listed in Table 2. The in-plane flutter mechanism is not detected with this reduced set of eigenmodes, being necessary to consider up to 20 modes (6 rigid-body modes, 14 elastic modes) to identify this flutter mechanism.

It should be noted that an in-plane flutter mechanism based on aerodynamic potential methods cannot be detected due to the lack of vertical aerodynamic forces caused by in-plane motions. However, the flutter mode has a symmetrical bending contribution in addition to the in-plane motion which enables the detection of an in-plane flutter mechanism also when considering aerodynamic potential-based methods. This explains the significant deviations in the flutter speeds between NASTRAN and CFD Euler or CFD RANS (see also Fig. 12) for this flutter mechanism.

Fig. 11 shows the course of the damping curves as a comparison of ZAERO-based (blue), Euler-based (red) and RANS-based (green) flutter calculations. Here it can be clearly seen that the flutter speeds from CFD calculations are significantly lower than those provided by the ZAERO calculations. In particular, for the body-Freedom flutter mechanism and the anti-symmetric flutter mechanisms the slope of the damping coefficients versus the true airspeed are very pronounced close to the flutter point, indicating that the occurrence of this flutter mechanism is been very abrupt.

For the RANS computations only the rigid-body modes corresponding to heave and pitch motions were taken into account, leading to a different flutter speed when compared to the results obtained using the Euler computations For the Euler calculations the rigid-body modes show a contribution of the roll rigid-body mode of more than 30% for the antisymmetric flutter mechanism [18]. For the other flutter mechanisms (symmetric BFF and symmetric in-plane flapping) from the flutter modes show different eigenmode participations depending on the aerodynamic modeling method considered (RANS, Euler).

The damping for the in-plane flutter mechanism, which was determined using CFD-RANS, shows a progression that may again cross the zero line from above at higher speeds. This means that the damping becomes effective for higher speeds. However, this behavior is not observed if additional eigenmodes are taken into account.

Fig. 12 shows the flutter speed evolution in Equivalent Air Speed as a function the altitude for different aerodynamic modeling approaches. The blue curves show the reference solutions, calculated with NASTRAN [25]. The red curves represent the results of the Euler calculations [16]. Contrasted with these curves are the green curves from the CFD RANS calculations.

It can be seen that the flutter speeds as obtained with NASTRAN/DLM approach the values predicted on the basis of Euler and RANS-generated GAF matrices with increasing altitude and thus decreasing dynamic pressure.

Especially in the subsonic regime ($Ma = 0.2, 0.4$) and for low altitudes, the flutter speeds of the Body-Freedom- and antisymmetric flutter mechanisms as predicted by NASTRAN/DLM-based methods deviate significantly from those predicted by the RANS computations. This is due to the reduced set of eigenmodes used

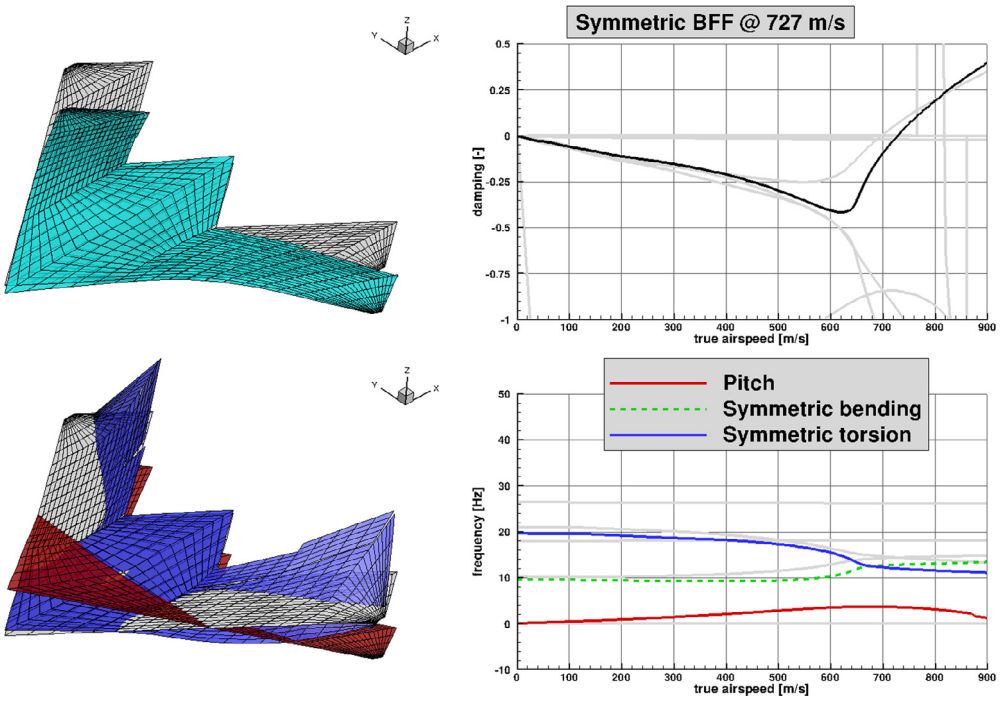

(a) Symmetric Body-Freedom-Flutter (8 eigenmodes considered)

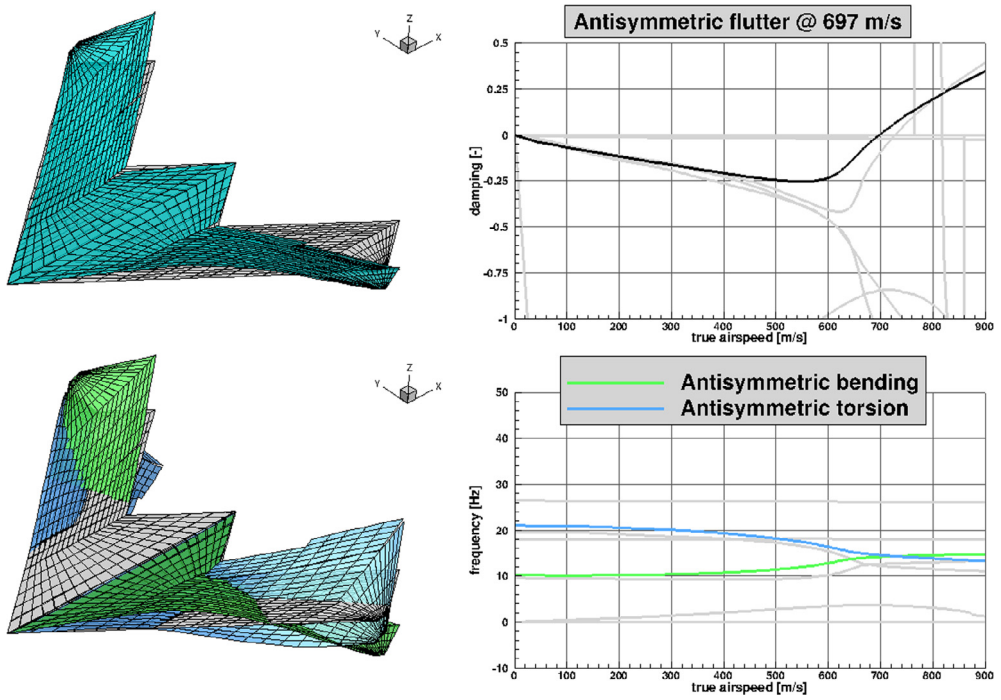

(b) Antisymmetric Flutter (8 eigenmodes considered)

Fig. 10. Flutter curves of the detected flutter mechanisms at Ma = 0.8 for ZONA6.

for the RANS calculations. As a result, the participations of higher-frequency elastic modes or other rigid-body modes (rolling mode) are not taken into account.

Furthermore, it should be noted that the flutter speed for the antisymmetric flutter mechanism from RANS calculations in the supersonic range is significantly lower than those based on the DLM and Euler computations. Again, the reason for this is that the RANS calculations were performed with a reduced mode set.

There is a fairly good correlation between the Euler and RANS calculations at the flutter speeds for the in-plane flutter mechanism in the mean Mach number range. Only small deviations appear at small and transonic Mach numbers for low altitudes. If the Mach number is further reduced the flutter speed produced by the CFD-based computations is nearly the same. Overall, it has been shown that a lower flutter speed is obtained with CFD-based flutter calculations when compared with aerodynamic potential methods.

Finally, for all cases investigated the considered flying wing configuration has sufficient flutter stability within a wide Mach number range since all flutter speeds are outside the extended flight envelope.

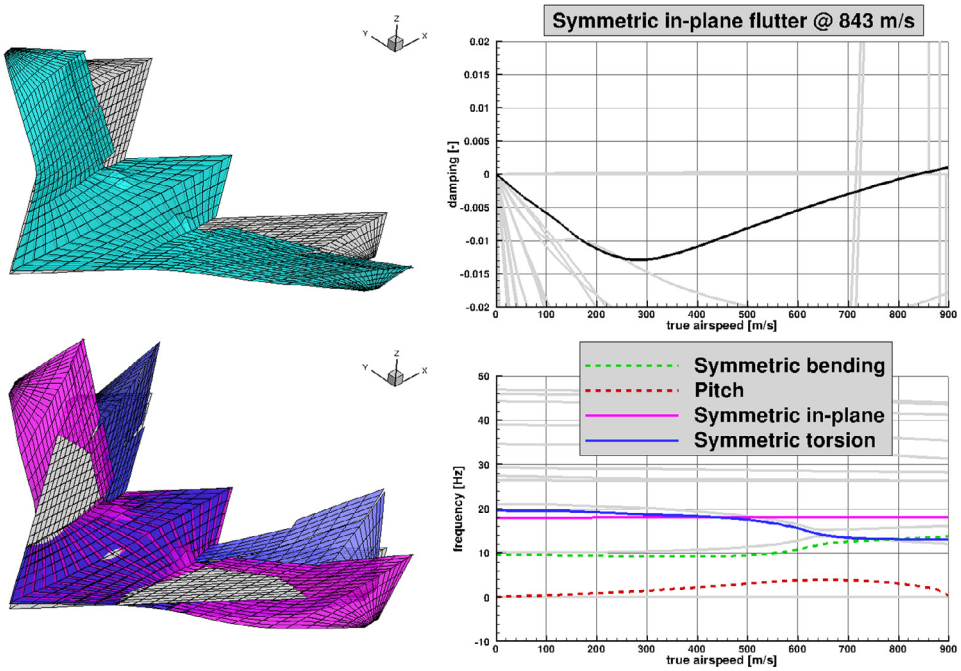

(c) Symmetric in-plane Flutter (20 eigenmodes considered)

Fig. 10. (*continued*)

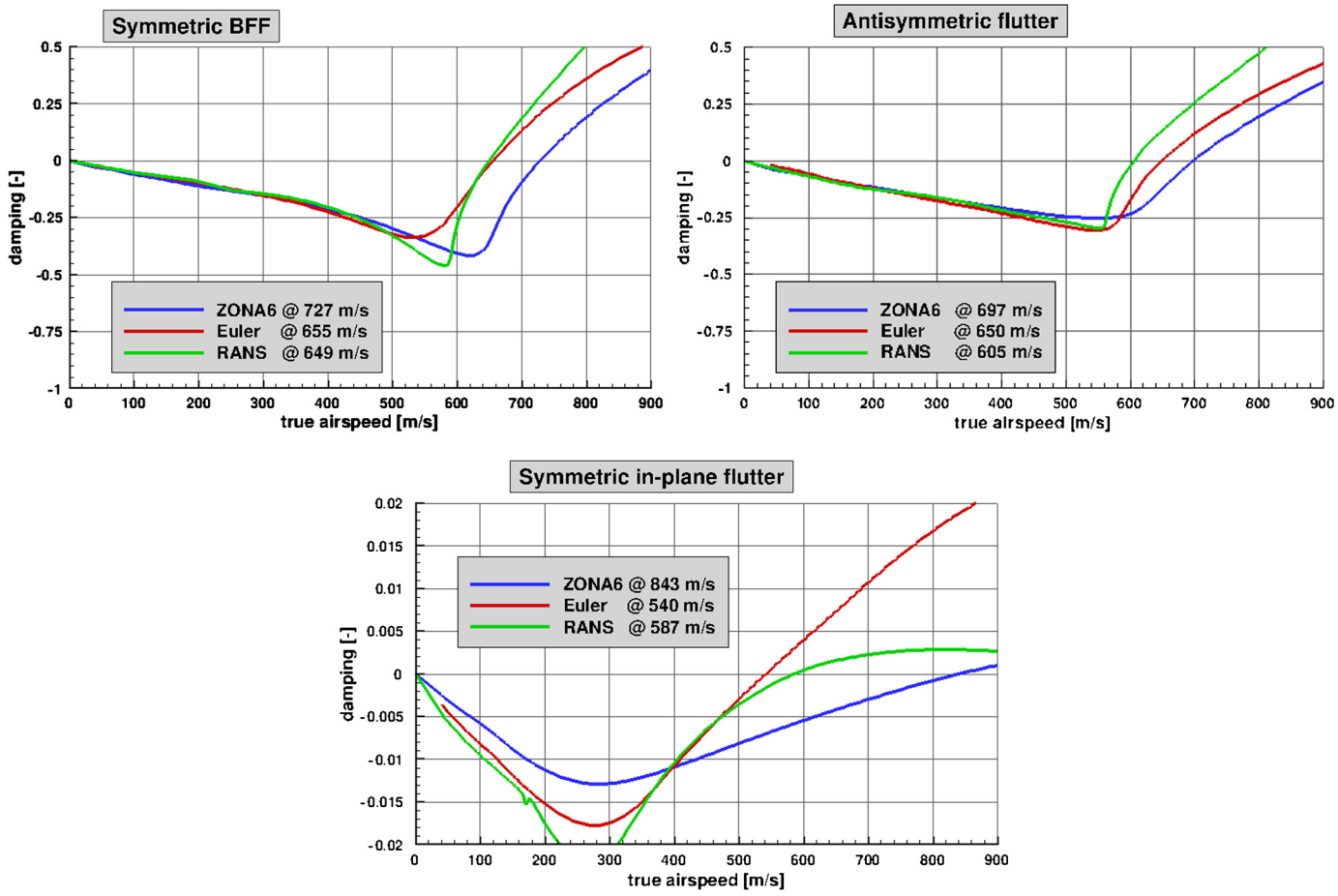

Fig. 11. Comparison of damping curves between ZAERO, Euler (with 20 modes considered) and CFD RANS (8 Modes).

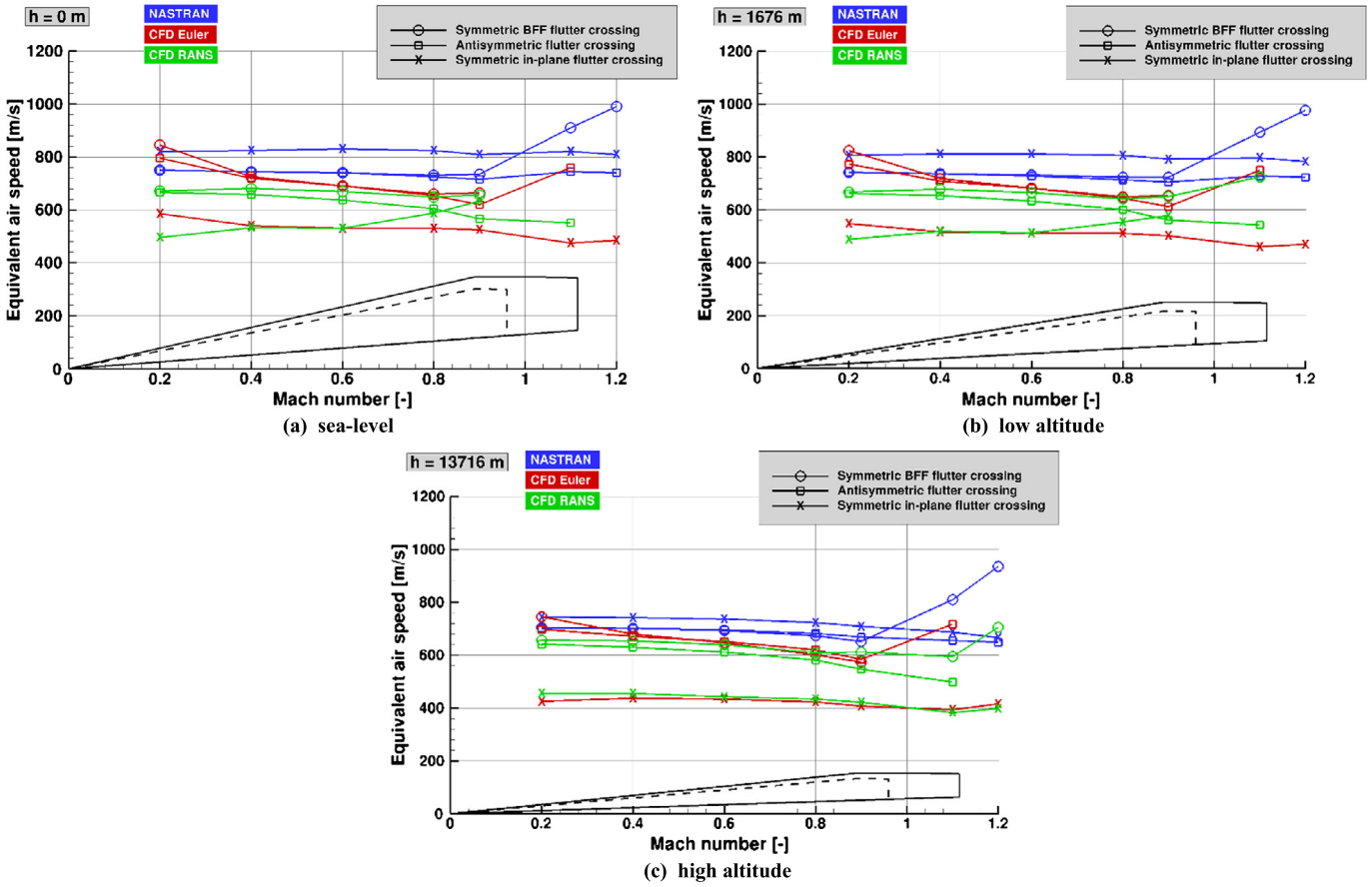

Fig. 12. Flutter velocities for different altitudes dependent on the used model.

4. Conclusion and outlook

Extensive investigations were carried out to determine the flutter stability of a flying wing configuration using the example of the F19 model. For this purpose, three different aerodynamic modeling approaches were used. These were DLM-based fast methods as well as CFD procedures (Euler and RANS). The DLM/ZONA51 methods as commonly used in the industrial environment were used as the reference solution.

For the RANS-based method (TAU-pulse) and the Euler-based method (AER-SDNS), several process chains were created that range from the generation of suitable computational grids, the generation of initial steady converged solutions, the calculation of unsteady aerodynamic forces and the determination of flutter curves for a wide variety of Mach numbers together with the corresponding flutter mechanisms. The same flutter mechanisms were detected, regardless of the methods used. On the contrary, the prediction of the flutter speeds show clear differences depending on the aerodynamic model used. This concerns in particular the in-plane flutter mechanism.

In the future, further studies will be carried out in order to investigate the influence of steady angles of attack or vortex-dominated flow with the subsequent flow separation patterns. Due to the appearing nonlinearities, flutter mechanisms can arise which have not been detected in the investigations carried out here, existing flutter mechanisms can be switched off and thus different flutter speeds can be expected. Such further investigations may extend or complete the understanding of the physical principles behind the occurring flutter mechanisms.

Declaration of Competing Interest

There is no competing interest.

Acknowledgements

The structural and mass models of the F19 configuration were created by Arne Voss at the DLR Institute for Aeroelasticity in Göttingen and made available for this work.

References

[1] I.E. Garrick, W.H. Reed, Historical development of aircraft flutter, J. Aircr. 18 (11) (1981).
[2] Wesley Li, Chan-Gi Pak, Aeroelastic optimization study based on X-56A model, in: AIAA Atmospheric Flight Mechanics Conference, Atlanta, GA, USA, 2014.
[3] X-56A completes envelope clearance flights, http://www.nasa.gov/centers/armstrong/features/X-56A_milestone.html, Sept. 2 2015.
[4] www.centaursoft.com.
[5] M. Galle, Ein Verfahren zur numerischen Simulation kompressibler, reibungsbehafteter Strömungen auf hybriden Netzen, Diss., DLR-FB, pp. 99-04, 1999.
[6] T. Gerhold, O. Friedrich, J. Evans, Calculations of Complex Three-Dimensional Configurations Employing the DLR-TAU-Code, AIAA 97-0167, Reno, 1997.
[7] A. Voss, T. Klimmek, Design and sizing of a parametric structural model for a UCAV configuration for loads and aeroelastic analysis, in: Deutscher Luft- und Raumfahrtkongress, 2015.
[8] ZAERO User's Manual, 2014.
[9] MIL-A-8870C, Military Specification: Airplane Strength and Rigidity Vibration, Flutter, and Divergence, 1993.
[10] D.D. Liu, D.K. James, P.C. Chen, A.S. Pototzky, Further studies of harmonic gradient method for supersonic aeroelastic applications, J. Aircr. 28 (9) (1991) 598–605.
[11] P.C. Chen, D.D. Liu, A harmonic gradient method for unsteady supersonic flow calculations, J. Aircr. 22 (5) (1985) 371–379.

[12] W.P. Rodden, E.H. Johnson, MSC.NASTRAN Aeroelastic Analysis User's Guide Version 68, The MacNeal-Schwendler Corporation Publication, 1994.
[13] P. Garcia-Fogeda, D.D. Liu, A harmonic potential panel method for flexible bodies in unsteady supersonic flow, AIAA paper 86-007, Aerospace Science Meeting, 24th, Reno, NV, 1986, also: J. Aircr. 24 (6) (1987) 833–840.
[14] P.C. Chen, H.W. Lee, D.D. Liu, Unsteady subsonic aerodynamics for bodies and wings with external stores including wake effect, J. Aircr. 30 (5) (1993) 618–628.
[15] MSC Nastran 2017 Dynamic Analysis User's Guide, 2017.
[16] C. Vidy, L. Katzenmeier, M. Winter, Ch. Breitsamter, Verification of the use of small-disturbance CFD aerodynamics in flutter and gust analyses for simple to highly complex configurations, in: International Forum on Aeroelasticity and Structural Dynamics, Saint Petersburg, Russia, 2015.
[17] ZAERO Theoretical Manual, 2014.
[18] D. Schaefer, Flutter Analysis of DLR-F19 Considering Rigid Body Motion and Transonic Aerodynamic Forces, Master Thesis, 2016.
[19] E. Kreiselmaier, B. Laschka, Small disturbance Euler equations (SDEE): an efficient and accurate tool for unsteady load predictions at all mach numbers, J. Aircr. 37 (5) (2000) 770–778.
[20] L. Katzenmeier, C. Vidy, C. Breitsamter, Correction technique for quality improvement of doublet lattice unsteady loads by introducing CFD small disturbance aerodynamics, J. Aeroel. Struct. Dyn. 5 (1) (2017).
[21] N. Kroll, et al., DLR project digital-X: towards virtual aircraft design and flight testing based on high-fidelity methods, CEAS Aeronaut. J. 7 (2016) 3–27.
[22] P.R. Spalart, S.R. Allmaras, A one-equation turbulence model for aerodynamic flows, in: 30th Aerospace Sciences Meeting & Exhibit, Reno, 1992.
[23] USAF, Standard Atmosphere, 1976.
[24] H.J. Hassig, An approximate true damping solution of the flutter equation by determinant iteration, J. Aircr. 8 (11) (1971).
[25] D. Schaefer, C. Vidy, C. Mack, J. Arnold, Assessment of Body-Freedom Flutter for an Unmanned Aerial Vehicle, Deutscher Luft- und Raumfahrtkongress, 2015.